

Multiscale modeling of lung mechanics: from alveolar microstructure to pulmonary function

Daniel E. Hurtado^{a,b,c,1}, Nibaldo Avilés-Rojas^{a,b}, Felipe Concha^a

^a*Department of Structural and Geotechnical Engineering, School of Engineering, Pontificia Universidad Católica de Chile, Santiago, Chile, Vicuña Mackenna 4860, Santiago, Chile*

^b*Institute for Biological and Medical Engineering, Schools of Engineering, Medicine and Biological Sciences, Pontificia Universidad Católica de Chile, Vicuña Mackenna 4860, Santiago, Chile*

^c*Institute for Medical Engineering and Science, Massachusetts Institute of Technology, Cambridge, MA, 02140, USA*

Abstract

The mechanical behavior of the lungs has long been associated with the structural properties of alveoli in pulmonary medicine. However, this structure-function relationship has mostly been qualitative, as experimentation in real lungs is costly and limited by ethical standards. Here we present a poromechanical multiscale model that connects key alveolar features with organ-level function. To this end, we first revisit an asymptotic homogenization framework for finite-deformation poromechanics and formulate fine-scale and coarse-scale problems that govern lung mechanics. We further inform the coarse-scale problem using a tetrakaidecahedron micromechanical model for the alveolar response at the fine scale that strongly depends on the alveolar-wall elastic modulus and the initial alveolar porosity. Based on this formulation, we construct a non-linear finite element model from anatomical geometries to simulate the response of human lungs connected to a mechanical ventilator under pressure-controlled and volume-controlled protocols. We show that the predicted signals for airway pressure, airway flow, and lung volume capture the dynamic waveform characteristics observed in human lungs. Further, we demonstrate that lung behavior, measured in terms of respiratory-system compliance, strongly depends on the alveolar-wall elasticity and alveolar porosity. In particular, we show that variations in these microstructural parameters result in marked changes in compliance that follow the structure-function relations observed in lungs with pulmonary fibrosis and emphysema, two prevalent chronic respiratory diseases. We envision that our multiscale lung model can enhance current *in silico* efforts to experimentation in respiratory research and provide a computational framework for clinically-relevant simulations.

Keywords: Structure-function, Finite-Deformation Homogenization, Lung Mechanics, Tetrakaidecahedron

*Corresponding Author: Daniel E. Hurtado, email address: dhurtado@ing.puc.cl, Phone: +562 2354 4207

1. Introduction

Breathing is a critical function of the human body that enables life, during which fresh air travels from the nose and mouth to the alveoli and back. To this end, millions of interconnected alveolar units that constitute the lung tissue cyclically stretch to bring air in and out of the deforming lungs. This interaction across scales explains why lung function is strongly influenced by alveolar microstructural features, constituting yet another remarkable example of the structure-function paradigm that pervades biological systems. Not surprisingly, structural alterations in alveoli manifest at the organ level as impaired lung function [17]. One example of this multiscale relation is idiopathic pulmonary fibrosis, a progressive and devastating disease with a survival time from diagnosis of just three years [46]. In fibrotic lungs, the alveolar extracellular matrix remodels by experiencing an increased deposition of collagen fibers, which stiffens alveolar walls [57]. As a result, lung compliance, or its ability to deform to increase the lung volume, is significantly reduced, hindering the ability of the patient to breathe. Another example is pulmonary emphysema, a highly prevalent disease where alveolar walls are destroyed. The reduction of alveolar walls gives rise to enlarged airspaces within the lung tissue. This alteration in tissue morphology results in a softer lung, as revealed by the abnormally high values of organ compliance in emphysematous lungs [37, 53]. These clinical observations, where structural changes in the tissue alter the organ-level mechanics, motivate the development of multiscale models that can explain the relationship between alveolar microstructure and pulmonary function.

Traditionally, computational simulations of lung mechanics model the interaction between acinar respiratory units and airway flow using fractal lumped models [44, 47, 48, 55, 56]. In this approach, airway trees are reconstructed from medical images or created using fractal network algorithms. Most of these models assume elastic spherical acinar elements at the terminals of the fractal network to represent parenchymal tissue response. Fractal lumped models deliver tractable computational simulations that have proven insightful in the study of regional ventilation. However, by construction, they fail to seamlessly account for the mechanical interaction between adjacent acinar units, questioning the accuracy of the ventilation-deformation coupling. An alternative modeling framework is continuum poromechanics, which directly accounts for the local interaction between gas and solid phases that coexist within the lung tissue [29]. Poromechanical models using anatomical geometries have been recently explored to study the airway-lung coupling [7], and the interaction of the lung with the thoracic cage under quasi-static conditions [40]. A recent contribution from our group constructs a whole-organ finite-element model to predict clinically-relevant respiratory variables typically monitored in the lungs of patients connected to mechanical ventilation [2]. While poromechanical models have demonstrated their potential in lung mechanics simulations, they are limited in that they assume phenomenological constitutive models that cannot connect microstructural parameters with tissue and organ response [15].

Multiscale modeling offers a theoretical framework for predicting the mechanical response of porous materials by explicitly considering the underlying microstructure [11, 30, 41].

Finite-deformation formulations of multiscale poromechanics have been developed in the literature using asymptotic homogenization arguments. In this context, Collis et al. [13] derived a system of effective equations describing the flow, elastic deformation, and transport in an active poroelastic medium. After asymptotic expansion, they obtained a Biot-like [8, 9] model that explicitly considers details of the microstructure and admits finite growth and deformations. Based on a similar homogenization approach, Miller and Penta [35] up-scale the fine-scale behavior of non-linear porous elastic composites, in which a solid matrix interacts with various phases and is filtered by a fluid flowing through the pores. These approaches offer a sound theoretical framework for finite-deformation poroelastic simulations. However, their use in specific applications requires the development of appropriate unit-cell microstructures, and their implementation in numerical simulations remains underexplored.

In this work, we formulate and implement a multiscale poromechanical model of lung function that effectively upscales the alveolar behavior into the whole-organ response. To this end, in Section 2, we draw concepts from finite-deformation multiscale poroelasticity to arrive at coarse-scale (tissue) governing equations that are informed by fine-scale (alveolar) problems. We also develop a weak formulation of the poromechanical model that is suitable for non-linear finite-element discretizations. We revisit the tetrakaidecahedron (TKD) unit-cell model developed in a previous contribution to represent the alveolar tissue microstructure [14] in Section 2.5 and adapt it in a form suitable for large-scale problems. In section 3, we present numerical simulations of an anatomical model of a lung connected to a mechanical ventilator and study how microstructural features influence organ response. Finally, we discuss the advantages and limitations of the proposed lung model in Section 4, along with an outlook of future work.

2. Multiscale formulation of finite-deformation poroelasticity for lung mechanics

2.1. Composite domain problem

In the following, we consider the poromechanical framework developed by Collis et al. [13] as a starting point. Let Ω_X^ξ be a composite domain in the material (reference) configuration and $\Omega_x^\xi := \boldsymbol{\varphi}^\xi(\Omega_X^\xi)$ the respective spatial (current) configuration, where the superscript ξ denotes the length scale associated to the microstructure, and $\boldsymbol{\varphi}^\xi : \Omega_X^\xi \times \mathbb{R} \rightarrow \mathbb{R}^3$ is the composite deformation mapping. We define the composite displacement field as $\mathbf{u}^\xi := \boldsymbol{\varphi}^\xi - \mathbf{X}^\xi$. The composite deformation-gradient tensor field is then computed as $\mathbf{F}^\xi := \frac{\partial \boldsymbol{\varphi}^\xi}{\partial \mathbf{X}^\xi}$, and the composite jacobian is determined as $J^\xi := d\Omega_x^\xi/d\Omega_X^\xi = \det \mathbf{F}^\xi$. We assume the material composite domain to be constituted by a solid phase $\Omega_{X_S}^\xi$ and a fluid (gas) phase $\Omega_{X_F}^\xi$, such that $\Omega_X^\xi = \Omega_{X_S}^\xi \cup \Omega_{X_F}^\xi$ and $\Omega_{X_S}^\xi \cap \Omega_{X_F}^\xi = \emptyset$. The solid and fluid domains in the spatial configuration are denoted by $\Omega_{x_S}^\xi$ and $\Omega_{x_F}^\xi$, respectively. Neglecting inertial effects and gravity forces the conservation of linear momentum for the solid and fluid phases are given by

$$\nabla_X \cdot \mathbf{P}_S^\xi = \mathbf{0} \quad \text{in } \Omega_{X_S}^\xi, \quad (1)$$

$$\nabla_x \cdot \boldsymbol{\sigma}_F^\xi = \mathbf{0} \quad \text{in } \Omega_{x_F}^\xi, \quad (2)$$

respectively. Mass conservation of the fluid phase requires that

$$\nabla_x \cdot \mathbf{v}^\xi = 0 \quad \text{in } \Omega_{x_F}^\xi, \quad (3)$$

where $\mathbf{P}_S^\xi : \Omega_{X_S}^\xi \rightarrow \mathbb{R}^{3 \times 3}$ is the composite first Piola-Kirchhoff stress-tensor field for the solid phase, $\boldsymbol{\sigma}_F^\xi : \Omega_{x_F}^\xi \rightarrow \mathbb{R}^{3 \times 3}$ is the composite Cauchy stress-tensor field for the fluid phase, and $\mathbf{v}^\xi : \Omega_{x_F}^\xi \rightarrow \mathbb{R}^3$ is the fluid velocity field. In this work, the solid phase representing the alveolar tissue is assumed to behave as a hyperelastic material [15]. The fluid phase, which represents the gas in the alveolar airspace, is assumed to behave as an incompressible Newtonian fluid, whose Cauchy stress tensor is then written as

$$\boldsymbol{\sigma}_F^\xi = -p^\xi \mathbf{I} + \mu (\nabla_x \mathbf{v}^\xi + (\nabla_x \mathbf{v}^\xi)^T), \quad (4)$$

with $p^\xi : \Omega_{x_F}^\xi \times \mathbb{R} \rightarrow \mathbb{R}$ the composite fluid pressure, $\mu \in \mathbb{R}_+$ the fluid viscosity, and \mathbf{I} the identity tensor. In the context of multiscale fluid-structure interaction problems, the interplay between solid and fluid phases at their common interface is governed by the continuity of stress and velocities [13]. To state these relations, we pull back the fluid Cauchy stress tensor to the material configuration using the Nanson-Piola transformation, which yields

$$\mathbf{P}_F^\xi = (\boldsymbol{\sigma}_F^\xi \mathbf{H}^\xi) \circ \boldsymbol{\varphi}^\xi, \quad (5)$$

where $\mathbf{H}^\xi := \mathcal{J}^\xi (\mathbf{F}^\xi)^{-T}$. Then, the compatibility of traction vectors on the solid-fluid interface is given by

$$\mathbf{P}_S^\xi \mathbf{N} = \mathbf{P}_F^\xi \mathbf{N} \quad \text{on } \partial\Omega_{X_{FS}}, \quad (6)$$

where \mathbf{N} is the unitary normal vector on the solid-fluid interface $\partial\Omega_{X_{FS}}$. For kinematic compatibility, we enforce that

$$\frac{\partial \mathbf{u}^\xi}{\partial t} = \mathbf{v}^\xi \circ \boldsymbol{\varphi}^\xi \quad \text{on } \partial\Omega_{X_{FS}}^\xi. \quad (7)$$

Similar to previous contributions, we normalize all governing equations to work with dimensionless fields [35]. By doing so, the expressions above still hold except for Eq. (4), which now reads

$$\boldsymbol{\sigma}_F^\xi = -p^\xi \mathbf{I} + \xi^2 \mu (\nabla_x \mathbf{v}^\xi + (\nabla_x \mathbf{v}^\xi)^T), \quad (8)$$

where we note that the viscosity μ is scaled by a factor ξ^2 , which can be related to Stokes flow in porous media [41].

Following a two-scale homogenization approach [4], we substitute the composite domain as the Cartesian product of a coarse-scale domain and a fine-scale domain, see Figure 1. Let Ω_X be the coarse-scale domain in the reference configuration, and Θ_Y be the locally periodic fine-scale domain with coordinates $\mathbf{X} \in \Omega_X$ and $\mathbf{Y} \in \Theta_Y$, respectively. We approximate the solid composite domain as the space product $\Omega_{X_S}^\xi = \Omega_X \times \Theta_{Y_S}$, and the fluid composite domain as $\Omega_{X_F}^\xi = \Omega_X \times \Theta_{Y_F}$, where Θ_{Y_S} and Θ_{Y_F} are the solid and fluid phases of the fine-scale domain in the Material configuration and are such that $\Theta_Y = \Theta_{Y_S} \cup \Theta_{Y_F}$ and

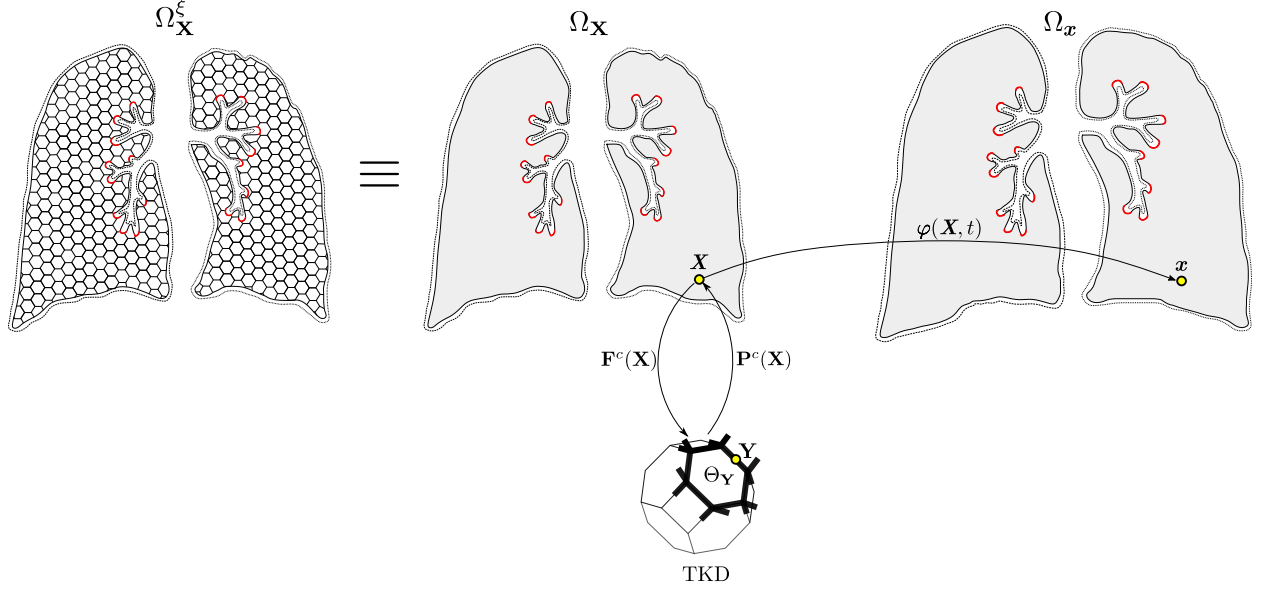


Figure 1: Multiscale modeling approach for lung composite domain Ω_X^ξ . Each point \mathbf{X} in the coarse scale Ω_X is informed by a fine-scale TKD micromechanical model with domain Θ_Y . Spatial configuration Ω_x results from applying the φ mapping to the coarse-scale reference configuration.

$\Theta_{Y_S} \cap \Theta_{Y_F} = \emptyset$. Furthermore, Θ_{y_S} and Θ_{y_F} represent the spatial configuration for the solid and fluid fine-scale domains, respectively. Let $\hat{\mathbf{X}}$ be unit-cell centroid. We note that the fine-scale and coarse-scale coordinates are related through the length scale ξ ($0 < \xi \ll 1$) such that $\mathbf{Y} = \frac{1}{\xi}(\mathbf{X} - \hat{\mathbf{X}})$. From this relationship, we note that if we express a field in terms of the unit-cell centroid, that is, $f^\xi(\mathbf{X}) = f(\hat{\mathbf{X}}, \mathbf{Y})$, then by the chain rule we have [19, 20]

$$\frac{\partial f^\xi(\mathbf{X})}{\partial X_j} = \frac{1}{\xi} \frac{\partial f(\hat{\mathbf{X}}, \mathbf{Y})}{\partial Y_j}. \quad (9)$$

2.2. Homogenization analysis: asymptotic expansion

We begin our derivation from the classical two-scale asymptotic homogenization theory, where a generic field h is expanded as

$$h^\xi(\mathbf{X}) = h^{(0)}(\mathbf{X}, \mathbf{Y}) + \xi h^{(1)}(\mathbf{X}, \mathbf{Y}) + \xi^2 h^{(2)}(\mathbf{X}, \mathbf{Y}) + \mathcal{O}(\xi^3). \quad (10)$$

For the case of the displacement field, the ξ^0 -term fields are assumed not to depend on \mathbf{Y} [19]. Based on this, we expand the displacement field as

$$\mathbf{u}^\xi(\mathbf{X}) = \mathbf{u}^{(0)}(\mathbf{X}) + \xi \mathbf{u}^{(1)}(\mathbf{X}, \mathbf{Y}) + \xi^2 \mathbf{u}^{(2)}(\mathbf{X}, \mathbf{Y}) + \mathcal{O}(\xi^3). \quad (11)$$

Following the large-strain approach taken in [19, 20], we perform Taylor expansions around the unit-cell centroid $\hat{\mathbf{X}}$, and rewrite (12) as

$$\mathbf{u}^\xi(\mathbf{X}) = \hat{\mathbf{u}}^{(0)}(\hat{\mathbf{X}}) + \xi \hat{\mathbf{u}}^{(1)}(\hat{\mathbf{X}}, \mathbf{Y}) + \xi^2 \hat{\mathbf{u}}^{(2)}(\hat{\mathbf{X}}, \mathbf{Y}) + \mathcal{O}(\xi^3), \quad (12)$$

where the components of the displacement fields are

$$\hat{u}_i^{(0)}(\hat{\mathbf{X}}) = u_i^{(0)}(\hat{\mathbf{X}}), \quad (13)$$

$$\hat{u}_i^{(1)}(\hat{\mathbf{X}}, \mathbf{Y}) = u_i^{(1)}(\hat{\mathbf{X}}, \mathbf{Y}) + \left. \frac{\partial u_i^{(0)}}{\partial X_j} \right|_{\hat{\mathbf{X}}} Y_j, \quad (14)$$

$$\hat{u}_i^{(2)}(\hat{\mathbf{X}}, \mathbf{Y}) = u_i^{(2)}(\hat{\mathbf{X}}, \mathbf{Y}) + \left. \frac{\partial u_i^{(1)}}{\partial X_j} \right|_{\hat{\mathbf{X}}} Y_j + \frac{1}{2} \left. \frac{\partial^2 u_i^{(0)}}{\partial X_j \partial X_k} \right|_{\hat{\mathbf{X}}} Y_j Y_k, \quad (15)$$

where in the last expressions we have used Einstein's notation, with repeated indices in one monomial implying summation. For convenience, we define the coarse-scale displacement field by

$$\mathbf{u}^c(\hat{\mathbf{X}}) := \hat{\mathbf{u}}^{(0)}(\hat{\mathbf{X}}), \quad (16)$$

and the fine-scale displacement field by

$$\mathbf{u}^f(\hat{\mathbf{X}}, \mathbf{Y}) := \hat{\mathbf{u}}^{(1)}(\hat{\mathbf{X}}, \mathbf{Y}), \quad (17)$$

Applying the derivative rule (9) and collecting ξ -powers terms, we obtain the coarse-scale and fine-scale deformation gradients [14]

$$\mathbf{F}^c(\hat{\mathbf{X}}) := \nabla_X \mathbf{u}^c(\hat{\mathbf{X}}) + \mathbf{I}, \quad (18)$$

$$\mathbf{F}^f(\hat{\mathbf{X}}, \mathbf{Y}) := \nabla_X \mathbf{u}^f(\hat{\mathbf{X}}, \mathbf{Y}) + \mathbf{I}, \quad (19)$$

respectively. Further, we expand the solid First Piola-Kirchhoff stress field as

$$\mathbf{P}_S^\xi = \hat{\mathbf{P}}_S^{(0)}(\hat{\mathbf{X}}, \mathbf{Y}) + \xi \hat{\mathbf{P}}_S^{(1)}(\hat{\mathbf{X}}, \mathbf{Y}) + \mathcal{O}(\xi^2). \quad (20)$$

For convenience, we define the fine-scale First Piola-Kirchhoff stress tensor as $\mathbf{P}_S^f := \mathbf{P}_S^{(0)}$ [19]. Then, substituting (20) into (1), applying the derivative rule (9), and matching ξ -powers terms we get

$$\nabla_Y \cdot \mathbf{P}_S^f(\hat{\mathbf{X}}, \mathbf{Y}) = \mathbf{0} \quad \text{in } \Omega_X \times \Theta_{Y_S}, \quad (21)$$

$$\nabla_X \cdot \mathbf{P}_S^f(\hat{\mathbf{X}}, \mathbf{Y}) + \nabla_Y \cdot \mathbf{P}_S^{(1)}(\hat{\mathbf{X}}, \mathbf{Y}) = \mathbf{0} \quad \text{in } \Omega_X \times \Theta_{Y_S}, \quad (22)$$

and we note that (21) defines the *governing equation for the fine-scale solid problem*, see also [14].

For the formulation of the fluid problem, we expand the composite fluid pressure and velocity fields as

$$p^\xi(\mathbf{x}) = \hat{p}^{(0)}(\hat{\mathbf{x}}, \mathbf{y}) + \xi \hat{p}^{(1)}(\hat{\mathbf{x}}, \mathbf{y}) + \mathcal{O}(\xi^2), \quad (23)$$

$$\mathbf{v}_i^\xi(\mathbf{x}) = \hat{\mathbf{v}}_i^{(0)}(\hat{\mathbf{x}}, \mathbf{y}) + \xi \hat{\mathbf{v}}_i^{(1)}(\hat{\mathbf{x}}, \mathbf{y}) + \mathcal{O}(\xi^2), \quad (24)$$

respectively, where

$$\hat{p}^{(0)}(\hat{\mathbf{X}}, \mathbf{Y}) = p^{(0)}(\hat{\mathbf{X}}, \mathbf{Y}), \quad \hat{p}^{(1)}(\hat{\mathbf{X}}, \mathbf{Y}) = \left. \frac{\partial p^{(0)}}{\partial X_j} \right|_{\hat{\mathbf{X}}} Y_j + p^{(1)}(\hat{\mathbf{X}}, \mathbf{Y}), \quad (25)$$

$$\hat{v}_i^{(0)}(\hat{\mathbf{X}}, \mathbf{Y}) = v_i^{(0)}(\hat{\mathbf{X}}, \mathbf{Y}), \quad \hat{v}_i^{(1)}(\hat{\mathbf{X}}, \mathbf{Y}) = \left. \frac{\partial v_i^{(0)}}{\partial X_j} \right|_{\hat{\mathbf{X}}} Y_j + v_i^{(1)}(\hat{\mathbf{X}}, \mathbf{Y}). \quad (26)$$

Using arguments analogous to those considered in for the solid problem, it follows from the multiscale expansion of equation (2) that

$$\nabla_y \cdot \boldsymbol{\sigma}_F^{(0)}(\hat{\mathbf{x}}, \mathbf{y}) = \mathbf{0} \quad \text{in } \Omega_x \times \Theta_{y_F}, \quad (27)$$

$$\nabla_x \cdot \boldsymbol{\sigma}_F^{(0)}(\hat{\mathbf{x}}, \mathbf{y}) + \nabla_y \cdot \boldsymbol{\sigma}_F^{(1)}(\hat{\mathbf{x}}, \mathbf{y}) = \mathbf{0} \quad \text{in } \Omega_x \times \Theta_{y_F}, \quad (28)$$

where we had expanded the fluid Cauchy stress tensor as

$$\boldsymbol{\sigma}_F^\xi = \hat{\boldsymbol{\sigma}}_F^{(0)}(\hat{\mathbf{x}}, \mathbf{y}) + \xi \hat{\boldsymbol{\sigma}}_F^{(1)}(\hat{\mathbf{x}}, \mathbf{y}) + O(\xi^2). \quad (29)$$

Further, expanding equation (8) and matching ξ -powers terms results in

$$\boldsymbol{\sigma}_F^{(0)}(\hat{\mathbf{x}}, \mathbf{y}) = -p^{(0)}(\hat{\mathbf{x}}, \mathbf{y}) \mathbf{I} \quad \text{in } \Omega_x \times \Theta_{y_F}, \quad (30)$$

$$\boldsymbol{\sigma}_F^{(1)}(\hat{\mathbf{x}}, \mathbf{y}) = -p^{(1)}(\hat{\mathbf{x}}, \mathbf{y}) \mathbf{I} + \mu (\nabla_y \mathbf{v}^{(0)}(\hat{\mathbf{x}}, \mathbf{y}) + (\nabla_y \mathbf{v}^{(0)}(\hat{\mathbf{x}}, \mathbf{y}))^T) \quad \text{in } \Omega_x \times \Theta_{y_F}, \quad (31)$$

and substituting these expressions into (27) and (28) we obtain

$$-\nabla_y p^{(0)}(\hat{\mathbf{x}}, \mathbf{y}) = \mathbf{0} \quad \text{in } \Omega_x \times \Theta_{y_F}, \quad (32)$$

$$-\nabla_y p^{(1)}(\hat{\mathbf{x}}, \mathbf{y}) + \mu \nabla_y \cdot \nabla_y \mathbf{v}^{(0)}(\hat{\mathbf{x}}, \mathbf{y}) - \nabla_x p^{(0)}(\hat{\mathbf{x}}, \mathbf{y}) = \mathbf{0} \quad \text{in } \Omega_x \times \Theta_{y_F}. \quad (33)$$

From (32) we conclude that $p^{(0)} = p^{(0)}(\hat{\mathbf{x}})$. Then, we define the coarse-scale pressure and fine-scale pressure as $p^c(\hat{\mathbf{x}}) := p^{(0)}(\hat{\mathbf{x}})$ and $p^f(\hat{\mathbf{x}}, \mathbf{y}) := p^{(1)}(\hat{\mathbf{x}}, \mathbf{y})$, respectively.

Asymptotic expansion and power matching on the fluid mass conservation equation (3) yields

$$\nabla_y \cdot \mathbf{v}^{(0)}(\hat{\mathbf{x}}, \mathbf{y}) = 0 \quad \text{in } \Omega_x \times \Theta_{y_F}, \quad (34)$$

$$\nabla_x \cdot \mathbf{v}^{(0)}(\hat{\mathbf{x}}, \mathbf{y}) + \nabla_y \cdot \mathbf{v}^{(1)}(\hat{\mathbf{x}}, \mathbf{y}) = 0 \quad \text{in } \Omega_x \times \Theta_{y_F}, \quad (35)$$

and we define the fine-scale velocity as $v^f(\hat{\mathbf{x}}, \mathbf{y}) := v^{(0)}(\hat{\mathbf{x}}, \mathbf{y})$.

Finally, we apply asymptotic expansion and match ξ -power terms for the stress compatibility given by (6) to obtain

$$\mathbf{P}_S^{(0)} \mathbf{N} = \left(\boldsymbol{\sigma}_F^{(0)} \mathbf{H}^{(0)} \right) \circ \boldsymbol{\varphi}(\hat{\mathbf{X}}, \mathbf{Y}) \mathbf{N} \quad \text{on } \partial\Theta_{Y_{FS}}, \quad (36)$$

$$\mathbf{P}_S^{(1)} \mathbf{N} = \left(\boldsymbol{\sigma}_F^{(0)} \mathbf{H}^{(1)} + \boldsymbol{\sigma}_F^{(1)} \mathbf{H}^{(0)} \right) \circ \boldsymbol{\varphi}(\hat{\mathbf{X}}, \mathbf{Y}) \mathbf{N} \quad \text{on } \partial\Theta_{Y_{FS}}, \quad (37)$$

and, proceeding analogously, from the velocity compatibility (7) we obtain that

$$\frac{\partial \mathbf{u}^{(0)}(\hat{\mathbf{X}})}{\partial t} = \mathbf{v}^{(0)} \circ \boldsymbol{\varphi}(\hat{\mathbf{X}}, \mathbf{Y}) \quad \text{on } \partial\Theta_{Y_{FS}}, \quad (38)$$

$$\frac{\partial \mathbf{u}^{(1)}(\hat{\mathbf{X}}, \mathbf{Y})}{\partial t} = \mathbf{v}^{(1)} \circ \boldsymbol{\varphi}(\hat{\mathbf{X}}, \mathbf{Y}) \quad \text{on } \partial\Theta_{Y_{FS}}. \quad (39)$$

2.3. Upscaling relations and coarse-scale governing problems

To establish a relation between fine and coarse scale problems, we consider (22). Integrating in the solid fine-scale domain, using the interface boundary conditions, and assuming periodicity in the purely solid and purely fluid boundaries yields

$$\int_{\Theta_{Y_S}} \nabla_X \cdot \mathbf{P}_S^f d\Theta_{Y_S} - \int_{\Theta_{Y_F}} \nabla_Y \cdot \mathbf{P}_F^{(1)} d\Theta_{Y_F} = \mathbf{0}. \quad (40)$$

Transforming (28) to the Material configuration and using (30) for the leading-order fluid stress tensor, we obtain

$$\nabla_Y \cdot \mathbf{P}_F^{(1)} = \nabla_X \cdot (P^c \mathbf{H}^{(0)}), \quad (41)$$

where $P^c = p^c \circ \boldsymbol{\varphi}$. Inserting this expression into equation (40), taking the average of each term, and noting that P^c does not depend on the fine scale, the coarse-scale linear momentum conservation reads

$$\nabla_X \cdot (\mathbf{P}_S^c - P^c \mathbf{H}^c) = \mathbf{0} \quad \text{in } \Omega_X, \quad (42)$$

where

$$\mathbf{P}_S^c = \frac{1}{\|\Theta_Y\|} \int_{\Theta_{Y_S}} \mathbf{P}_S^f d\Theta_{Y_S}, \quad (43)$$

$$\mathbf{H}^c = \frac{1}{\|\Theta_Y\|} \int_{\Theta_{Y_F}} \mathbf{H}^{(0)} d\Theta_{Y_F}. \quad (44)$$

In particular, we note that (43) provides an upscaling relation for the solid response. Following a standard poroelasticity formulation, we will assume the fluid contribution to the stress tensor defined in (44) to be an isotropic tensor in the current configuration (Terzaghi effective stress principle), such that it represents the hydrostatic effect of pore pressure, i.e.,

$$\mathbf{H}^{(0)} = J^C (\mathbf{F}^c)^{-T}. \quad (45)$$

Based on this consideration, the coarse-scale linear-momentum conservation equation takes the form

$$\nabla_X \cdot \mathbf{P}_S^{eff} = \mathbf{0} \quad \text{in } \Omega_X, \quad (46)$$

where the coarse-scale effective stress tensor is defined by

$$\mathbf{P}_S^{eff} = \mathbf{P}_S^c - J^c P^c (\mathbf{F}^c)^{-T}. \quad (47)$$

To derive the coarse-scale formulation for the fluid mass conservation, we integrate equation (35) and use the divergence theorem in its second term to write

$$\int_{\Theta_{y_F}} \nabla_x \cdot \mathbf{v}^f d\Theta_{y_F} + \int_{\partial\Theta_{y_F}} \mathbf{v}^{(1)} \cdot \mathbf{n} d\partial\Theta_{y_F} + \int_{\partial\Theta_{y_{FS}}} \mathbf{v}^{(1)} \cdot \mathbf{n} d\partial\Theta_{y_{FS}} = 0. \quad (48)$$

Using periodicity conditions and assuming that the velocity of the solid is negligible compared to that of the fluid, we obtain

$$\nabla_x \cdot \int_{\Theta_{y_F}} \mathbf{v}^f d\Theta_{y_F} = 0. \quad (49)$$

Following [19], we introduce the ansatz $\mathbf{v}^f = \mathbf{w} \nabla_x p^c$, with \mathbf{w} an auxiliary field, and take the average in the unit cell to arrive to

$$\nabla_x \cdot (\mathbf{k} \nabla_x p^c) = 0, \quad (50)$$

where

$$\mathbf{k} = \frac{1}{\|\Theta_y\|} \int_{\Theta_{y_F}} \mathbf{w} d\Theta_{y_F}. \quad (51)$$

Finally, performing a pull-back operation on (51), we arrive at the Material coarse-scale mass-balance equation

$$\nabla_X \cdot \left(J^c \mathbf{F}^{c^{-1}} \mathbf{K} \mathbf{F}^{c^{-T}} \nabla_X P^c \right) = 0 \quad \text{in } \Omega_X, \quad (52)$$

where $\mathbf{K} = \mathbf{k} \circ \boldsymbol{\varphi}$ the permeability tensor. We note that the computation of this tensor requires the solution of the auxiliary function \mathbf{w} on a unit-cell problem for the fluid phase. However, for simplicity, we assume a constant and isotropic permeability such that $\mathbf{K} = K \mathbf{I}$, with $K = 10^4 \text{ mm}^2/\text{kPa}\cdot\text{s}$ [2, 7].

At this point, we note that (52) corresponds to a steady-state problem from mass conservation. To consider the transient regime of airflow in the lungs, we add to this balance statement the variation of fluid mass measured in terms of a porosity field to arrive to

$$\frac{\partial \Phi}{\partial t} + \nabla_X \cdot \mathbf{Q}^c = 0 \quad \text{in } \Omega_X \times (0, T], \quad (53)$$

where

$$\mathbf{Q}^c = J^c \mathbf{F}^{c^{-1}} \mathbf{K} \mathbf{F}^{c^{-T}} \nabla_X P^c, \quad (54)$$

is the Material flux field, and Φ the Material porosity field, that for a media with incompressible solid and fluid phases can be further computed as

$$\Phi = J^c + \Phi_0 - 1 \quad (55)$$

where Φ_0 is the initial Material porosity [16, 33].

2.4. Weak formulation of the multi-scale fluid-solid problem

Collecting the coarse-scale governing equations and upscaling relations derived in previous sections, we state the strong formulation of the multiscale fluid-solid interaction problem

as follows: Find $\varphi^c : \Omega_X \times \mathbb{R} \rightarrow \mathbb{R}^3$ and $P^c : \Omega_X \times \mathbb{R} \rightarrow \mathbb{R}$ such that

$$\nabla_X \cdot \mathbf{P}_S^{eff} = \mathbf{0} \quad \text{in } \Omega_X \times (0, T] \quad (56)$$

$$\frac{\partial \Phi}{\partial t} + \nabla_X \cdot \mathbf{Q}^c = 0 \quad \text{in } \Omega_X \times (0, T] \quad (57)$$

$$\varphi^c = \varphi_0^c \quad \text{in } \partial\Omega_X \quad (58)$$

$$P^c = P_0^c \quad \text{on } \partial\Omega_X \quad (59)$$

$$\varphi^c = \bar{\varphi}^c \quad \text{on } \partial\Omega_X^\varphi \times (0, T] \quad (60)$$

$$\mathbf{P}_S^{eff} \cdot \mathbf{N} = \bar{\mathbf{T}}^c \quad \text{on } \partial\Omega_X^T \times (0, T] \quad (61)$$

$$P^c = \bar{P}^c \quad \text{on } \partial\Omega_X^P \times (0, T] \quad (62)$$

$$\mathbf{Q}^c \cdot \mathbf{N} = \bar{Q}^c \quad \text{on } \partial\Omega_X^Q \times (0, T], \quad (63)$$

where \mathbf{P}^{eff} and \mathbf{Q}^c are defined by Eqns. (47) and (54), respectively.

For the construction of a non-linear finite-element solution to this problem, we seek the associated weak formulation. To this end, we define the following trial and test function spaces

$$\mathcal{S}_{\varphi^c} := \{\varphi^c : \varphi^c \in H^1(\Omega_0, \mathbb{R}^3); \varphi^c = \bar{\varphi}^c \text{ on } \partial\Omega_X^\varphi\}, \quad (64)$$

$$\mathcal{V}_{\varphi^c} := \{\boldsymbol{\eta}^c : \boldsymbol{\eta}^c \in H^1(\Omega_0, \mathbb{R}^3); \boldsymbol{\eta}^c = \mathbf{0} \text{ on } \partial\Omega_X^\varphi\}, \quad (65)$$

$$\mathcal{S}_{P^c} := \{P^c \in H^1(\Omega_0, \mathbb{R}); P^c = \bar{P}^c \text{ on } \partial\Omega_X^P\}, \quad (66)$$

$$\mathcal{V}_{P^c} := \{q^c \in H^1(\Omega_0, \mathbb{R}); q^c = 0 \text{ on } \partial\Omega_X^P\}. \quad (67)$$

To derive the weak form associated to the linear momentum balance equation, we multiply (56) by $\boldsymbol{\eta}^c \in \mathcal{V}_{\varphi^c}$, apply integration by parts, use the boundary condition (61) and expand the expression for \mathbf{P}^{eff} to get the subproblem: Find $\varphi^c \in \mathcal{S}_{\varphi^c}$ and $P^c \in \mathcal{S}_{P^c}$ such that

$$\int_{\Omega_X} \mathbf{P}_S^c : \nabla_X \boldsymbol{\eta}^c \, d\Omega_X - \int_{\Omega_X} \left(J^c P^c (\mathbf{F}^c)^{-T} \right) : \nabla_X \boldsymbol{\eta}^c \, d\Omega_X - \int_{\partial\Omega_X} \mathbf{T}_S^c \cdot \boldsymbol{\eta}^c \, d\partial\Omega_X = 0, \quad (68)$$

for any $\boldsymbol{\eta}^c \in \mathcal{V}_{\varphi^c}$. For the case of the fluid coarse-scale problem, we multiply (57) by $q^c \in \mathcal{V}_{P^c}$, use the integration by parts theorem, and consider the boundary condition (63) to arrive at the weak equation

$$\int_{\Omega_X} \frac{\partial \Phi}{\partial t} q \, d\Omega_X - \int_{\Omega_X} \mathbf{Q}^c \cdot \nabla_X q \, d\Omega_X + \int_{\partial\Omega_X} \bar{Q}^c q \, d\partial\Omega_X = 0, \quad (69)$$

for any $q^c \in \mathcal{V}_{P^c}$.

The weak-form residuals (68) and (69) were discretized in time using a backward-Euler integration scheme. The space fields were discretized using a standard Galerkin finite-element (FE) formulation to obtain a dynamic multi-field FE problem [23, 27]. To solve this FE problem numerically, we developed an enhanced version of the FEniCS library [31], where functions solving the fine-scale problem were coupled to non-linear FE solvers. The element multi-field formulation considered a Taylor-Hood (P2-P1) interpolation scheme.

2.5. Fine-scale problem: The tetrakaidecahedron (TKD) model

To inform the coarse-scale constitutive relation defined by (43), the fine-scale solid problem needs to be solved first. In this work, for the fine-scale problem, we consider the tetrakaidecahedron (TKD) model proposed by Concha and Hurtado [14], which has been developed for alveolar microstructures. In the following, we summarize the main aspects of this micromechanical model.

The TKD geometry can be observed in Figure 1. Based on symmetry considerations [15], we consider a subregion of it, denoted as TKDr, which is representative of the entire TKD, and can also represent an infinitely periodic network of TKD elements. The TKDr is formed by strut elements that can only deform axially and whose strain energy density function is given by the NeoHookean incompressible energy density

$$W(\mathbf{F}) = \frac{\mu}{2} \{ \text{tr}(\mathbf{F}^T \mathbf{F}) - 3 \} - w(\det \mathbf{F} - 1), \quad (70)$$

where μ is the Lamé parameter and w is a Lagrange multiplier used to enforce the incompressibility constraint

$$\det \mathbf{F} = 1 \quad \text{in } \Theta_{Y_S}. \quad (71)$$

To solve the solid fine-scale problem, we reformulate the associated boundary value problem as a saddle-point variational problem which can be written as

$$\begin{aligned} \min_{\mathbf{u} \in \mathbf{u}_{adm}} \max_{w \in L^2(\Theta_{Y_S})} \int_{\Theta_{Y_S}} \left[\frac{\mu}{2} \left\{ \text{tr}[(\mathbf{I} + \nabla_o \mathbf{u}^f)^T (\mathbf{I} + \nabla_o \mathbf{u}^f)] - 3 \right\} - w(\det(\mathbf{I} + \nabla_o \mathbf{u}^f) - 1) \right] d\Theta_{Y_S} - \\ \int_{\partial\Theta_{Y_{SF}}} [\mathbf{u}^f \cdot P_{alv}^c \det(\mathbf{I} + \nabla_o \mathbf{u}^f) (\mathbf{I} + \nabla_o \mathbf{u}^f)^{-T} \mathbf{N}] dS, \end{aligned} \quad (72)$$

where ∇_o is the gradient operator concerning the Material configuration. To solve this variational problem, we represent the TKDr by a truss structure with a square cross-section and elements connected at joints in the intersections. We denote by \mathbf{Q}_e and \mathbf{q}_e the difference between end-node coordinates in the reference and current configuration for the e -th element, respectively. Let h_o and h_e be the reference and current cross-section dimension of an element, respectively, and $L_{eo} = \|\mathbf{Q}_e\|$ the reference length of the element. From these definitions, we define the axial and transverse stretch ratios of the e -th element by

$$\lambda_e := \frac{\|\mathbf{q}_e\|}{L_{eo}} \quad e = 1, 18, \quad (73)$$

$$\lambda_e^T := \frac{h_e}{h_o} \quad e = 1, 18, \quad (74)$$

respectively. Using these definitions, we can express the deformation gradient tensor of the e -th element in local coordinates as

$$\mathbf{F}_e = \begin{bmatrix} \lambda_e & 0 & 0 \\ 0 & \lambda_e^T & 0 \\ 0 & 0 & \lambda_e^T \end{bmatrix}. \quad (75)$$

The potential energy of the TDKr structure considers the contribution of each element's deformation (axial) energy, the work done by alveolar pressure acting on the surface of each element, and a rotational energy term for each joint of the structure. Then, the total potential energy can be written as

$$\Pi = \sum_{e=1}^{18} \Pi_e^{\text{axial}}(\mathbf{q}_e, \lambda_e^T, w_e) - \sum_{e=1}^{18} \Pi_e^{\text{pressure}}(\lambda_e^T; p^c) + \sum_{j \in \mathcal{J}} \Pi_j^{\text{rotational}}(\mathbf{q}_{j1}, \mathbf{q}_{j2}) \quad (76)$$

with the axial, pressure and rotational energies terms computed as [14]

$$\Pi_e^{\text{axial}}(\mathbf{q}_e, \lambda_e^T, w_e) = A_o L_{eo} \left\{ \frac{\mu}{2} (\lambda_e^2 + 2\lambda_e^{T^2} - 3) - w_e (\lambda_e (\lambda_e^T)^2 - 1) \right\}, \quad (77)$$

$$\Pi_e^{\text{pressure}}(\lambda_e^T; p_{alv}^c) = -2A_o L_{eo} P_{alv}^c \lambda_e (\lambda_e^{T^2} - \lambda_e^T), \quad (78)$$

$$\Pi_j^{\text{rotational}}(\mathbf{q}_{j1}, \mathbf{q}_{j2}) = \frac{1}{2} k_\theta \left\{ \frac{\mathbf{q}_{j1} \cdot \mathbf{q}_{j2}}{\|\mathbf{q}_{j1}\| \|\mathbf{q}_{j2}\|} - \frac{\mathbf{Q}_{j1} \cdot \mathbf{Q}_{j2}}{\|\mathbf{Q}_{j1}\| \|\mathbf{Q}_{j2}\|} \right\}^2, \quad (79)$$

respectively. In the previous equations w_e is the Lagrange parameter for the e -th element, k_θ is the rotational stiffness expressed as

$$k_\theta = \alpha \frac{EI}{2\delta}, \quad (80)$$

with α a rotational parameter to be fitted, $E = 3\mu$ is the alveolar-wall elastic modulus, I is the flexural inertia moment of a square cross-section, δ is the initial strut half-length, and A_0 the reference cross- sectional area, which can be computed as [15]

$$A_o = \frac{32\sqrt{2}(1 - f_o)\delta^2}{12 - 9d}, \quad (81)$$

where d is an overlapping parameter, to be calibrated, and

$$f_0 := 1 - \frac{|\Theta_{Y_S}|}{|\Theta_Y|}, \quad (82)$$

is the initial reference porosity of the lung microstructure.

The TKD model assumes as an input a principal deformation state. To account for this assumption, we apply the polar decomposition theorem on the coarse-scale deformation-gradient tensor, i.e. $\mathbf{F}^c = \mathbf{R}^c \mathbf{U}^c$, and consider the stretch tensor to take the form

$$\mathbf{U}^c = \begin{bmatrix} \lambda_1^c & 0 & 0 \\ 0 & \lambda_2^c & 0 \\ 0 & 0 & \lambda_3^c \end{bmatrix} \quad (83)$$

where $\lambda_1^c, \lambda_2^c, \lambda_3^c$ are the coarse-scale principal stretches. We further consider a reduced set of degrees of freedom \mathbf{r} for the TKDr structure, which can be related to the remaining

degrees of freedom from symmetry considerations. Then, the TKD nodal displacements can be expressed as

$$\mathbf{u}_i = \mathbf{u}_i(\mathbf{r}; \mathbf{U}^c) \quad \forall i = 1, 18 \quad (84)$$

Letting $\mathbf{w} = [w_1, \dots, w_{18}]^T$ and $\mathbf{l} = [\lambda_1^T, \dots, \lambda_{18}^T]$, we rewrite the variational principle (72) as the optimization problem

$$\min_{\mathbf{r} \in \mathbb{R}^3, \mathbf{l} \in \mathbb{R}^{18}} \max_{\mathbf{w} \in \mathbb{R}^{18}} \Pi(\mathbf{r}, \mathbf{l}, \mathbf{w}; \mathbf{U}^c, P_{alv}^c) \quad (85)$$

where the strut variables λ_e^T, w_e can be locally solved such that $\mathbf{l} = \mathbf{l}(\mathbf{r}; \mathbf{U}^c)$ and $\mathbf{w} = \mathbf{w}(\mathbf{r}; \mathbf{F}^c, P_{alv}^c)$. Thus, the minimization problem reduces to

$$\min_{\mathbf{r} \in \mathbb{R}^3} \Pi^{\text{eff}}(\mathbf{r}; \mathbf{U}^c, p_{alv}^c) = \Pi^{\text{eff}}(\mathbf{r}^*; \mathbf{U}^c, P_{alv}^c), \quad (86)$$

where \mathbf{r}^* corresponds to the solution of the effective minimization problem. Finally, to compute the stress state, we use Hill's Lemma for large deformations, so

$$\mathbf{P}^c = \frac{1}{V_0} \frac{D\Pi^{\text{eff}}}{D\mathbf{U}^c}(\mathbf{r}; \mathbf{U}^c, P_{alv}^c), \quad (87)$$

or equivalently,

$$\hat{\mathbf{P}}^c = \frac{1}{V_0} \left[\frac{\partial \Pi^{\text{eff}}(\mathbf{r}^*; \mathbf{U}^c, p_{alv}^c)}{\partial \mathbf{r}} : \frac{\partial \mathbf{r}}{\partial \mathbf{U}^c} + \frac{\partial \Pi^{\text{eff}}(\mathbf{r}^*; \mathbf{U}^c, P_{alv}^c)}{\partial \mathbf{U}^c} \right] \quad (88)$$

where V_0 is the initial TKDr volume. Since $\frac{\partial \Pi}{\partial \mathbf{r}}$ is evaluated at the solution of the minimization problem (86), and the coarse-scale principal stress tensor takes the form

$$\hat{\mathbf{P}}^c = \frac{1}{V_0} \frac{\partial \Pi^{\text{eff}}(\mathbf{r}^*; \mathbf{U}^c, P_{alv}^c)}{\partial \mathbf{U}^c}. \quad (89)$$

As a last step, we use the principal stresses in (89) to construct the coarse-scale Piola-Kirchhoff tensor as

$$\mathbf{P}^c = \sum_{\alpha=1}^3 \hat{P}_{\alpha}^c \hat{\mathbf{n}}_{\alpha} \otimes \hat{\mathbf{N}}_{\alpha}, \quad (90)$$

where $\{\hat{\mathbf{N}}_{\alpha}\}_{\alpha=1,2,3}$ and $\{\hat{\mathbf{n}}_{\alpha}\}_{\alpha=1,2,3}$ are the Material and spatial principal directions associated to \mathbf{F}^c .

3. Numerical simulations

3.1. Model setup

To demonstrate the capabilities of the proposed multiscale framework, we constructed a non-linear finite-element lung model using an anatomical geometry, see Figure 2. We obtained the lung domain by segmenting a thoracic computed-tomography image acquired

for a normal subject, see [25, 26] for more details. Based on the lung domain, we generated a tetrahedral lung mesh using the CGAL library [12]. The mechanical interaction of the lung tissue with the rib cage and the mediastinum was modeled through continuous elastic elements represented by a Robin boundary condition of the form

$$\bar{\mathbf{T}}^c(\mathbf{X}) = K_s \{\boldsymbol{\varphi}(\mathbf{X}) - \mathbf{X}\} \quad \text{on } \partial\Omega_X, \quad (91)$$

which applies to the entire lung boundary. In all simulations, we considered $K_s = 80 \cdot 10^{-3}$ kPa/mm, which has shown to deliver a chest-wall compliance value that falls within the range observed in normal subjects [2]. For the prescription of boundary conditions for the gas flow equation, we partitioned the lung boundary into the surface occupied by the visceral pleura and the surface that delimited the airway boundary, taken as the bronchi cross sections [2]. A no-flux Neumann boundary condition was prescribed on the visceral pleura surface in all cases. The choice of boundary condition on the airway boundaries depended on the ventilation mode studied, as we detail below.

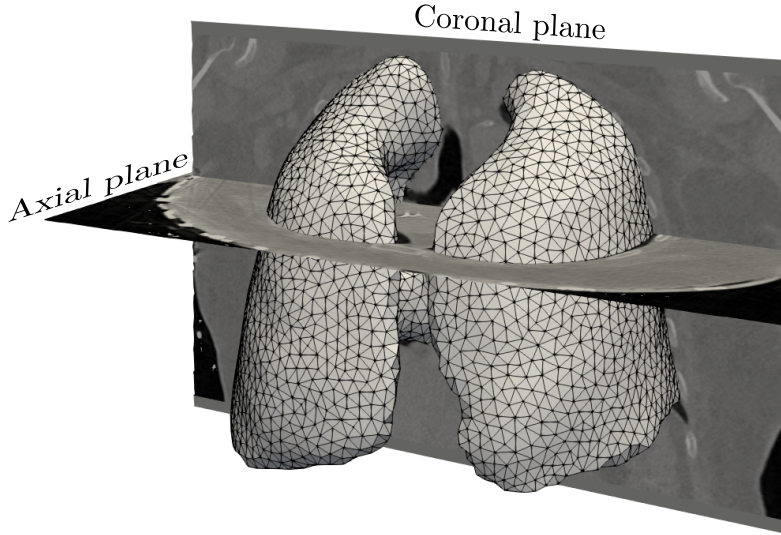


Figure 2: Anatomical finite-element mesh constructed for the lung simulations. The lung domain was determined from computed-tomography images of a normal human volunteer. Axial and coronal planes are shown for further reference.

To model the interaction between the lung and the air supplied by an external mechanical ventilator, we restricted airflow to take place only on the airway boundaries. Due to their relevance in the clinical setting, two modes of mechanical ventilation were considered in this study, we refer the reader to [2] for further details. In the pressure-controlled ventilation (PCV) mode, the mechanical ventilator imposes the airway-pressure signal, represented by a function denoted by $\bar{P}(t)$. At the beginning of inspiration, the pressure rapidly rises until

it reaches a peak value of 5 cm H₂O in 0.1 seconds, a pressure that is then maintained constant until the end of the inspiration phase, whose duration in total is 1 second. Then, this pressure is suddenly reduced to zero and maintained at this value for the next 2 seconds during the expiratory phase. In our simulations, this airway pressure signal was prescribed on the airway boundary. Once the simulation was carried out, the lung volume $V(t)$ and airway flow $\dot{V}(t)$ signals were computed during a post-processing step as

$$V(t) := \int_{\Omega_0} J d\Omega_0 - \int_{\Omega_0} d\Omega_0, \quad (92)$$

and

$$\dot{V}(t) := \int_{\Gamma_{\text{aw}}} \mathbf{Q} \cdot \mathbf{N} d\Gamma_{\text{aw}}, \quad (93)$$

where Γ_{aw} represents the airway boundary.

The volume-controlled ventilation (VCV) mode considers the case where the mechanical ventilator prescribes the airway flow so as to achieve a predefined level of maximum lung volume during each cycle. To this end, the airway flow $\bar{Q}(t)$ was set to a constant level for 1 second, followed by an inspiratory pause of 0.25 seconds of zero flow ($\bar{Q}(t) = 0$). After this pause, the boundary condition on the airway boundary changed to prescribed pressure, with $\bar{P}(t) = 0$ to allow for a passive expiration process. Using the results from the inspiratory phase, we computed the airway pressure $P_{\text{aw}}(t)$ and lung volume $V(t)$ signals as

$$P_{\text{aw}}(t) := \frac{1}{A_{\text{aw}}} \int_{\Gamma_{\text{aw}}} P_{\text{alv}}(\mathbf{X}, t) d\Gamma_{\text{aw}}, \quad (94)$$

$$V(t) := \int_{[0,t]} \bar{Q}(\tau) d\tau, \quad (95)$$

$$\dot{V}(t) := \bar{Q}(t). \quad (96)$$

During the expiratory phase, where pressure is prescribed, the lung volume and airway flow signals were computed according to Eqns. (92) and (93), respectively.

One physiological parameter of high clinical relevance in the respiratory-system compliance C_{rs} , which measures the ability of the lung to deform under a given pressure level. Using the lung mechanics signals provided by airway pressure, airway flow, and lung volume, we estimated the respiratory compliance by solving a least-square fit to a single-compartment model, see [2, 6] for further details.

To study the quasi-static behavior of the lung model, we constructed pressure-volume curves. To this end, the lung is inflated using small incremental volume steps produced by the prescription of constant airway flow, followed by a pause. Once a steady state is reached in a particular step, the resulting airway pressure is recorded. Based on this information, a pressure-volume curve was constructed for the baseline parameter values and for variations

Parameter	Baseline Value	Reference	5% Range	20% Range
Alveolar-wall elastic modulus μ [kPa]	10.33	[14, 42]	9.81 – 10.85	8.3 – 12.4
Initial alveolar porosity f_0 [-]	0.69	[14]	0.66 – 0.73	0.55 – 0.83
Rotational stiffness coefficient α [-]	10.05	[14]	–	–
Overlap coefficient d [-]	0.56	[14]	–	–

Table 1: Parameter values and ranges for the TKD alveolar model

in the alveolar-wall elasticity and alveolar porosity.

The TKD unit-cell model requires setting four parameters, which are considered homogeneous throughout the lung domain in this work. Table 1 show the values considered as the baseline for these parameters. To understand how variations in these microstructural features affect the macroscopic response, a sensitivity analysis was performed, considering parameter ranges for the alveolar-wall elasticity and initial alveolar porosity see Table 1. Variations on only these two parameters were selected due to their high influence on the tissue mechanical response [14].

3.2. Results

The spatiotemporal evolution of the jacobian and the alveolar pressure fields for the VCV baseline case are shown in Figure 3. We report three key time instants observed in a VCV mode cycle: the end of inspiration ($t_1 = 1.0$ s), the end of the inspiratory pause ($t_2 = 1.25$ s), and when half expiration has elapsed ($t_3 = 2.25$ s). The jacobian field displayed a heterogeneous distribution, reaching values of volumetric change up to 1.4 at the end of inspiration, see Figure 3(a). During expiration, the jacobian field approached a state of zero volumetric deformation. The alveolar pressure field followed a similar trend, with peak local values of roughly 8 cm H₂O at the end of inspiration, see Figure 3(b).

Figure 4 shows the spatiotemporal evolution of the hydrostatic stress and material porosity change fields. High heterogeneity was observed at the end of inspiration and inspiratory pause, with peak hydrostatic-stress values as high as 0.3 kPa, see Figure 4(a). Material porosity change displayed a spatial distribution and temporal evolution similar to the case of the jacobian field, with positive values everywhere throughout the lung, see Figure 4(b).

The airway pressure, flow, and lung volume signals were computed from the lung simulations for all the cases studied. Figure 5 shows these signals for the case of PCV mode, along with function envelopes that represent the variation of these signals for different levels of variation in the alveolar-wall elasticity and initial alveolar porosity. The flow waveform obtained for the baseline case displays a quick rise and drop following the beginning of the inspiratory ($t=0$ s) and expiratory ($t=1$ s) phases, respectively, followed by exponential decay towards zero flow. The time evolution of the volume can also be separated into a saturating exponential curve during the inspiratory phase, followed by an exponential decay towards the resting condition taking place during the expiratory phase. Variations in the alveolar-wall elasticity modulate these responses, as higher values of μ result in lower flow

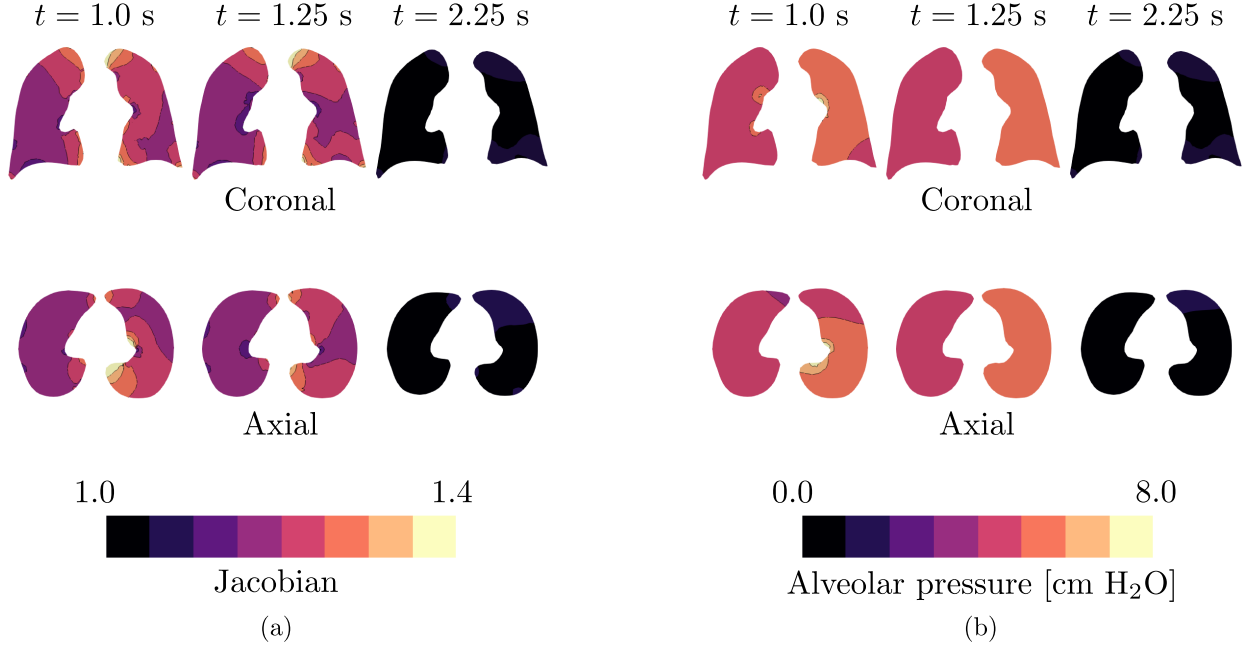


Figure 3: Temporal evolution during one respiratory cycle of volume-controlled mechanical ventilation in the baseline case: (a) jacobian field, and (b) alveolar pressure field. Fields are plotted on the current configuration.

and lung volume amplitudes, see Figure 5(a). In contrast, Figure 5(b) shows that an increase in material alveolar porosity causes larger amplitudes in the flow and lung volume signals.

Respiratory mechanics curves for the case of the VCV mode are shown in Figure 6. During the first phase of constant flow, the volume increases linearly up to the maximum lung volume, while the airway pressure evolves according to a saturating exponential. During the inspiratory (no-flow) pause, pressure rapidly decays to a plateau while lung volume is kept constant. For the expiratory phase, the rapid drop to zero airway pressure causes both the flow and volume to exponentially decay toward their resting values (zero). Figure 6(a) shows that increasing the alveolar-wall elasticity results in higher airway-pressure levels during the inspiratory phase, and lower lung volume values during the expiratory phase. In contrast to this trend, an increase in the initial alveolar porosity reduces the amplitude of the airway-pressure signal during inspiration and amplifies the amplitude of the lung-volume signal during expiration, see Figure 6(b).

To assess the dependence of lung mechanical parameters on microstructural features, we computed the respiratory-system compliance resulting from simulations that considered a range of values of the alveolar-wall elasticity and initial alveolar porosity, see Figure 7(a) and Figure 7(b), respectively. For a fixed baseline value of initial alveolar porosity, the respiratory-system compliance was found to monotonically decrease as alveolar-wall elasticity was increased. When the alveolar-wall elasticity was fixed, the respiratory-system compliance steadily increased as the initial alveolar porosity increased. Both relationships were non-linear in the parameter domain studied.

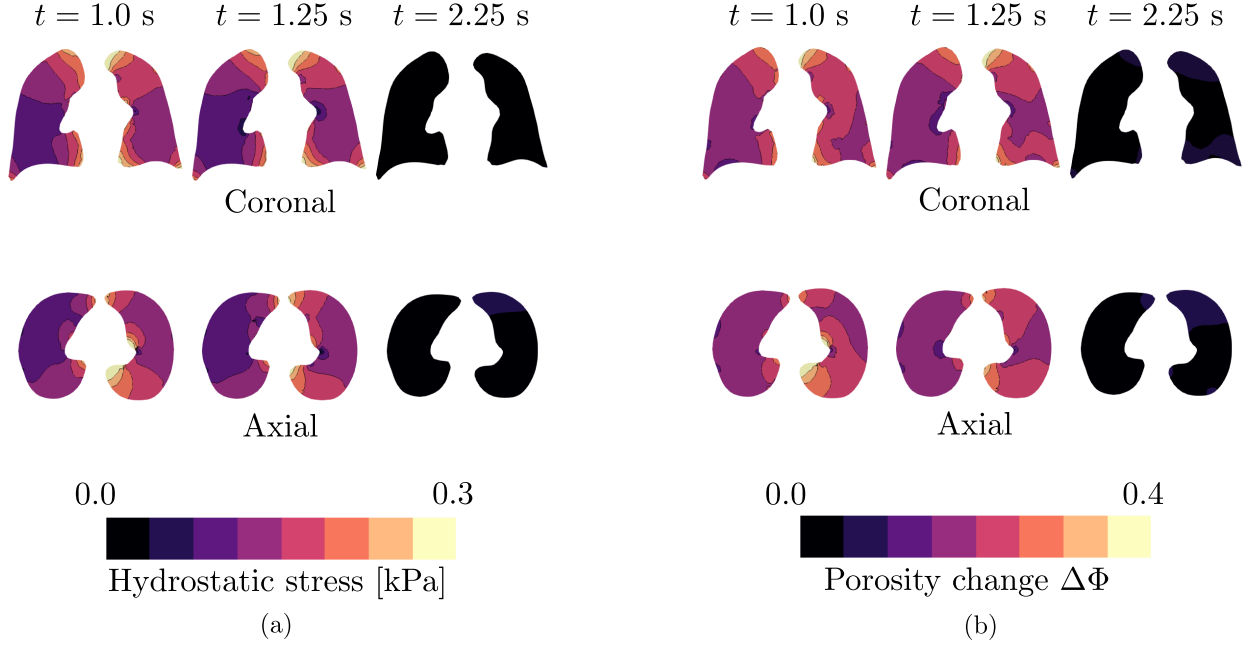


Figure 4: Temporal evolution during one respiratory cycle of volume-controlled mechanical ventilation in the baseline case: (a) hydrostatic stress field, and (b) material porosity change field. Fields are plotted on the current configuration

The influence of alveolar-wall elasticity and alveolar porosity on the quasi-static lung response is shown in Figures 8(a) and 8(b), respectively. In the case of alveolar-wall elasticity, greater values of μ resulted in lower lung volumes, for a given airway pressure. When f_0 was increased, lung volume increases for a given airway pressure. All pressure-volume curves displayed a non-linear shape.

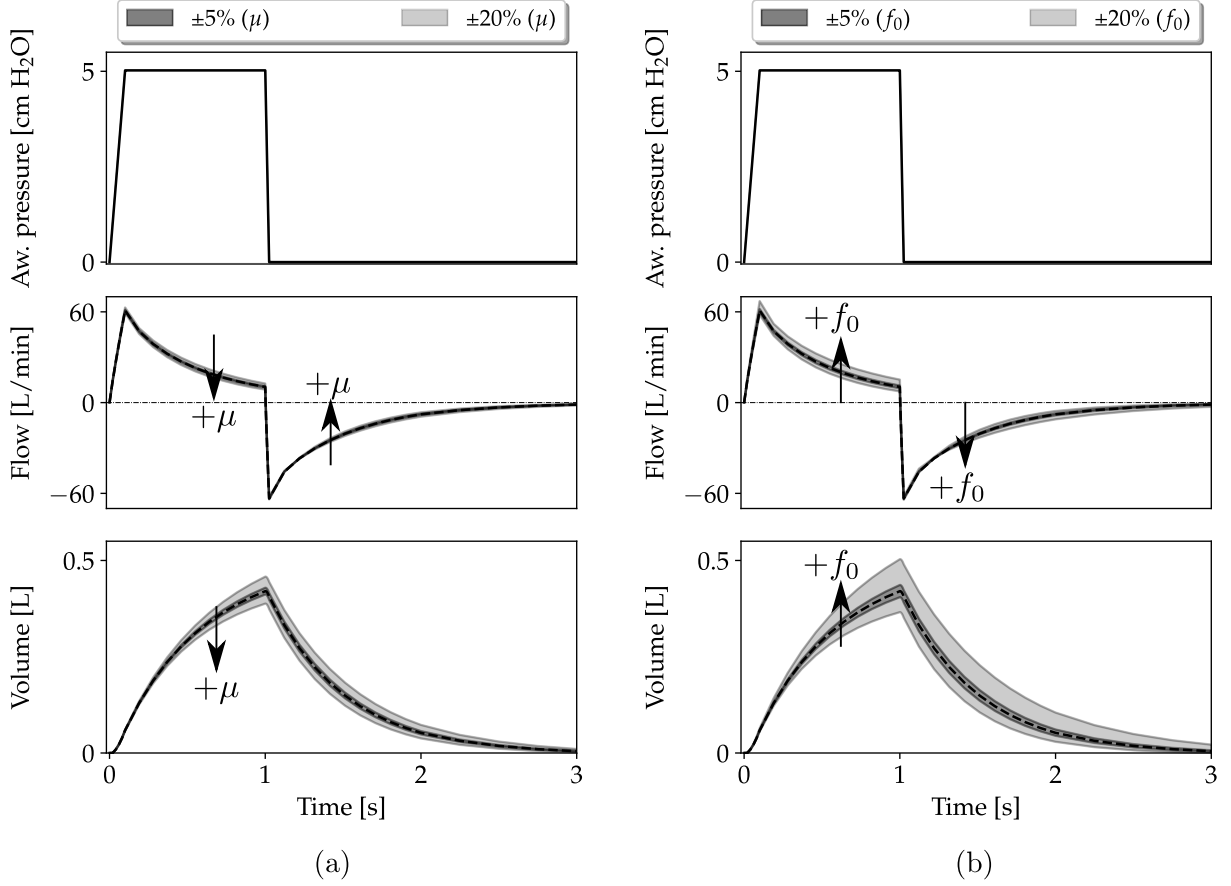


Figure 5: Respiratory signals and parameter sensitivity analysis for pressure-controlled mechanical ventilation: a) variations in the alveolar-wall elasticity, and b) variations in the initial alveolar porosity. Plots show the time evolution of airway pressure (top), flow (middle), and volume (bottom).

4. Discussion

In this work, we present a multiscale model of lung mechanics where alveolar microstructural parameters govern the organ-level mechanical response. Previous continuum models for the estimation of the multiscale lung response were based on a nested dynamic multiscale approach [58, 59]. This technique considers a two-scale deformation-driven homogenization framework, where the fine-scale problem is constructed from an idealized geometry of an alveolar ensemble and is solved using non-linear finite-element analysis. This approach, also known as direct numerical simulation, involves high computational demands as the fine-scale problem requires the solution of a non-linear problem with several thousands of degrees of freedom. From this perspective, the framework proposed in this work offers the advantage of being computationally efficient, as the TKD micromechanical model that informs the tissue level can be five orders of magnitude faster than direct numerical simulations while delivering a similar mechanical response [14]. This advantage enables the analysis of large-scale problems in reasonable computing times, effectively delivering multiscale predictions of

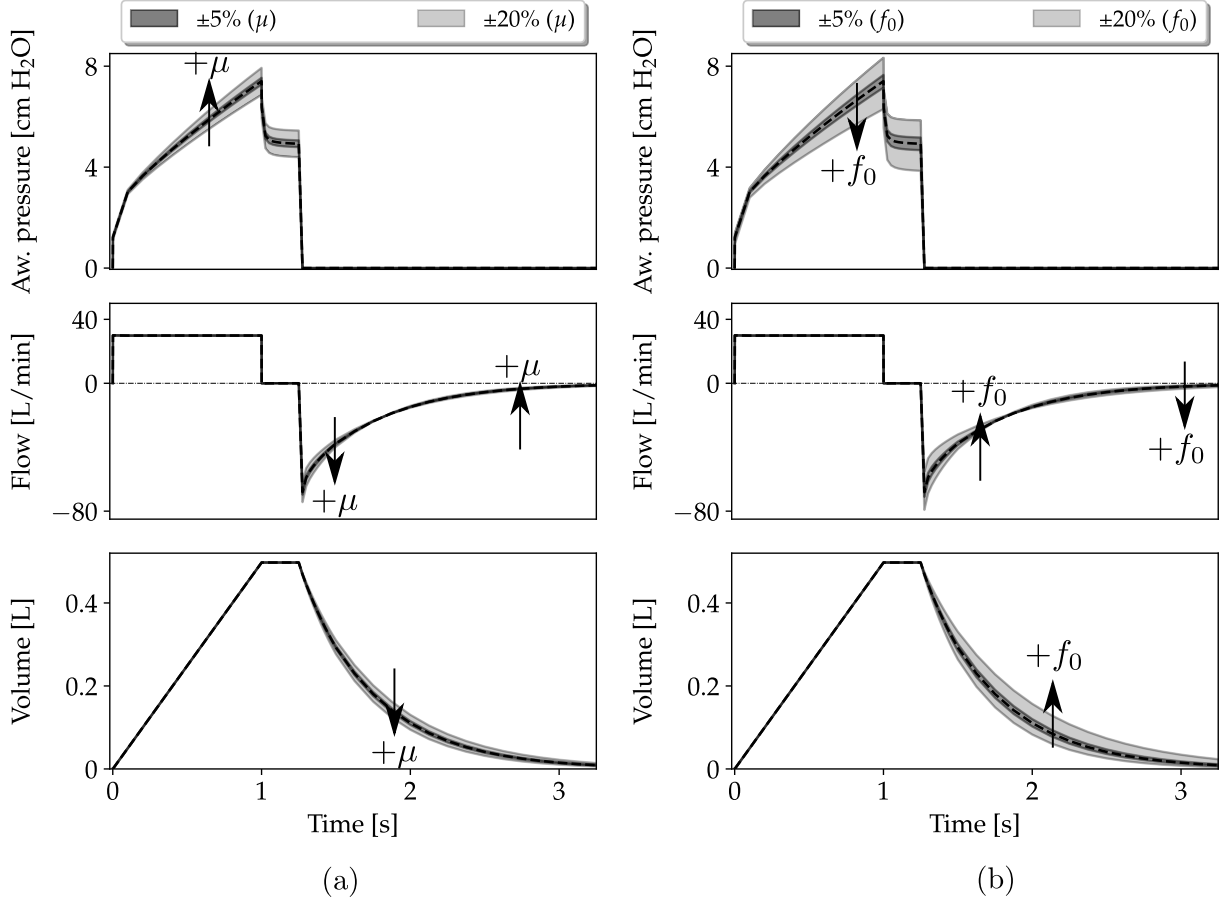


Figure 6: Respiratory signals and parameter sensitivity analysis for volume-controlled mechanical ventilation: a) variations in the alveolar-wall elasticity, and b) variations in the initial alveolar porosity. Plots show the time evolution of airway pressure (top), flow (middle), and volume (bottom).

deformation, alveolar pressure, stresses, and porosity fields on complex anatomical geometries that may require a large number of elements in their discretization, see Figures 3 and 4.

Another distinctive feature of our multiscale lung model is its poromechanical foundation, which directly accounts for the air-tissue interaction not captured by traditional deformation-driven lung models. In effect, lung tissue is a highly porous material everywhere in the lung [50], where air pressurizes the alveolar cavity inducing stresses and strains in the alveolar walls [1]. This tight interaction makes it necessary to couple the alveolar pressure with the tissue deformation [51]. We remark that previous contributions that have addressed lung mechanics using continuum poromechanical formulations consider phenomenological constitutive models for the tissue response [2, 7, 29, 40]. These models share the limitation that the constitutive parameters are determined from experimental data obtained from lung tissue samples, and thus they do not directly connect microstructural features to the tissue response. To the best of our knowledge, the present work constitutes one of the first

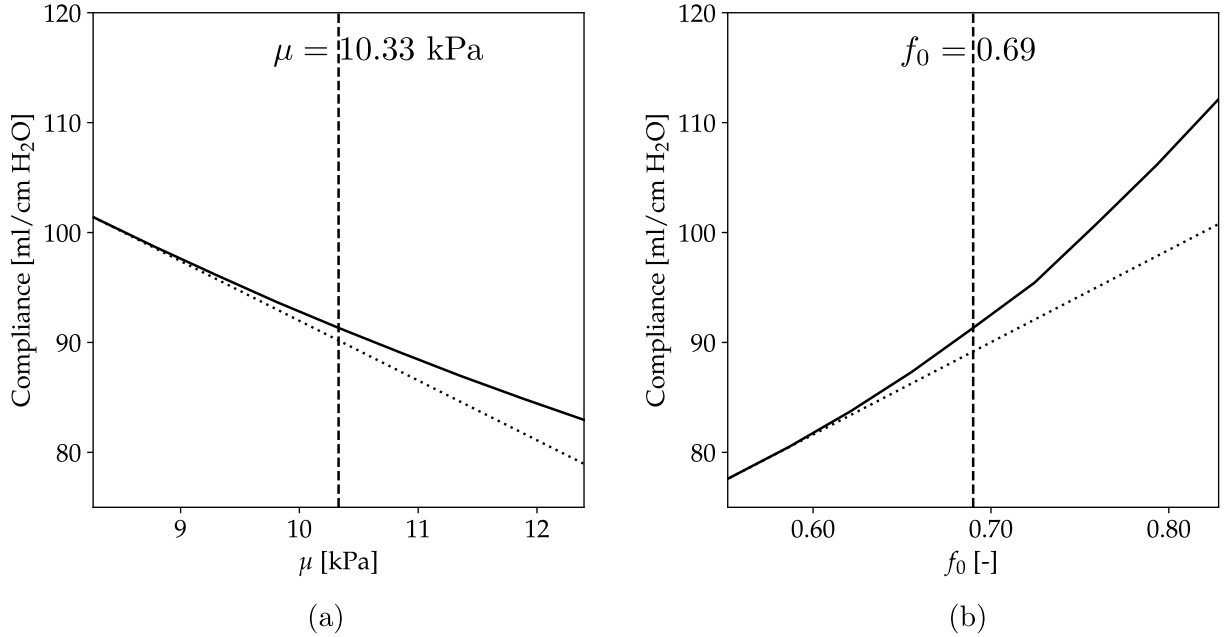


Figure 7: Parameter sensitivity analysis for the respiratory system compliance: a) influence of variations in the alveolar-wall elasticity μ , and b) influence of variations in the initial alveolar porosity f_0 . Baseline values of both parameters are indicated with a vertical dashed line. Dotted lines are included to visually assess the degree of non-linearity.

multiscale poromechanical models of the lung informed by alveolar structure and capable of predicting clinically-relevant respiratory mechanics parameters.

Airway pressure, flow, and lung volume are key respiratory signals in intensive care medicine, as they inform doctors in the clinical management of patients connected to mechanical ventilation [21]. Our multiscale lung model could predict these signals for the two modes of mechanical ventilation studied, PCV and VCV, see Figures 5 and 6, respectively. Remarkably, these signals agree with those observed in ventilated patients, see [32] for a review of respiratory mechanics signals. In the case of PCV, our model predicts flow spikes in response to pressure changes, followed by exponential decay toward zero. This translates into lung volume signals that exponentially increase and decrease, see Figure 5. For the VCV mode, lung volume linearly responds to a constant flow, followed by an inspiratory pause where a pressure plateau is reached, see Figure 6. After this pause, airway pressure drops to zero, creating a rapid spike followed by a decelerating flow response and an exponential decay in lung volume, which is typically observed in mechanically-ventilated patients [5]. Interestingly, when introducing variations in the microstructural parameters, we observe significant changes in the respiratory waveforms that can be related to clinical and experimental observations. For example, in patients under VCV, a decrease in the respiratory-system compliance results in larger peak amplitudes in flow and shorter time

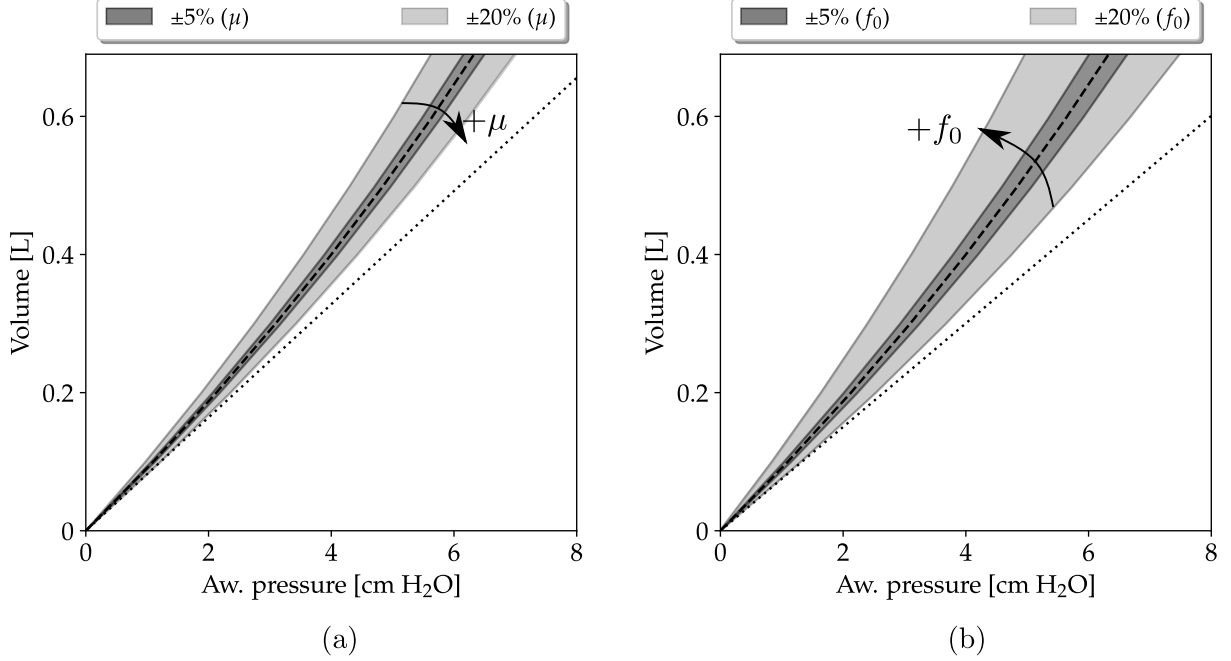


Figure 8: Quasi-static pressure-volume lung curves and parameter sensitivity analysis: a) variations in the alveolar-wall elasticity, and b) variations in the initial alveolar porosity. Dashed lines represent the baseline case. Dotted lines are included to visually assess the degree of non-linearity.

scales for the flow and volume during the exponentially-decaying expiratory phase, see [32]. Notably, these waveform changes are recovered by our simulations when the global compliance is reduced due to an increase in alveolar-wall elasticity or a decrease in the initial alveolar porosity, see Figure 6. Thus, we confirm that the proposed multiscale lung model can capture dynamic features of lung mechanics observed in human lungs.

Throughout this work, we have shown that the development of a multiscale lung model where the unit cell is constructed upon key parameters that describe the alveolar structure can relate changes in the organ-level function with variations in the microstructure, see Figure 7. While a continuous relation between respiratory compliance and parameters such as alveolar-wall elasticity or alveolar porosity is virtually impossible to achieve in an experimental setting, several investigations have established the connection between alveolar structure changes and their impact on lung function. Studies in normal and fibrotic human lungs have determined Young’s modulus of alveolar tissue using atomic-force microscopy [10], which results from enhanced collagen deposition [22, 52]. Results show that alveolar-wall elasticity in fibrotic lungs can be $8.4\times$ greater than that found in normal human lungs. At the same time, respiratory compliance in patients with idiopathic lung fibrosis reduces to 44% of the value predicted for a normal subject [43]. These findings confirm that stiffening of the alveolar wall is associated with significant decreases in the compliance of the respiratory system, a trend that is captured by our sensitivity analysis, see Figure 7(a). These multiscale relationships

have also been confirmed in animal models of bleomycin-induced pulmonary fibrosis [18]. Another way of assessing the multiscale structure-function relation in the lung is to consider animal studies of pulmonary emphysema. Parameswaran et al. [38] studied the mechanics and microstructure of normal and emphysematous rat lungs treated with porcine pancreatic elastase using micro-computed tomography. Lung function tests revealed an increase of 37% in the average dynamic compliance in the emphysema group when compared to the normal group.¹ Concurrently, the morphological image-based analysis revealed differences of up to $16\times$ in the alveolar airspace volume in emphysematous lungs when compared to normal ones. Noting that porosity directly relates to alveolar airspace volume, these results confirm that increases in alveolar porosity are associated with higher compliance values, a trend recovered by Figure 7(b). Given that compliance measures relative changes in lung volume and airway pressure, the increase of alveolar-wall elasticity is expected to stiffen the lung volume response, as shown in Figure 8(a). Analogously, increases in alveolar porosity translate into a softer lung volume response that is readily seen in Figure 8(b).

The work presented in this contribution offers many opportunities for further improvement. First, we note that only the hyperelastic response of lung tissue was addressed in the model formulation. Alveoli are lined by a thin layer of surfactant, a fluid that exerts surface tension on the alveolar walls [3]. Surface tension on alveolar walls is one of the main responsible for the hysteretic behavior of lungs and cannot be adequately represented by purely elastic constitutive models [45]. Future extensions may consider this inelastic contribution by enhancing the current TKD formulation to incorporate existing surfactant models that are based on alveolar surface changes Otis et al. [36], Saad et al. [49]. Second, for simplicity, we considered an incompressible Neo-Hookean model for the alveolar-wall mechanics. Such a constitutive law does not capture the increase of tangent elastic modulus as the walls deform, mainly attributed to the interaction between collagen and elastin fibers [34, 42, 54]. This stiffening effect can be incorporated into the TKD model by considering alternative constitutive relations for the structural elements that compose the TKD [28]. Finally, our simulations assumed a homogeneous spatial distribution of microstructural parameters. However, spatial variability in tissue ventilation, represented by porosity, is typically observed in lungs under respiratory failure, which is the most frequent condition for which mechanical ventilation is indicated [24]. Future versions of our multiscale lung model should focus on personalizing lung simulations based on available patient data, which can be achieved using inverse analysis on medical images [39].

Acknowledgements

This work was funded by the National Agency for Research and Development (ANID) of Chile through the grant FONDECYT Regular # 1220465. NA-R acknowledges the support of the graduate fellowship ANID BECAS/DOCTORADO NACIONAL 21212320.

¹In [38], mechanical function is assessed in terms of average dynamic elastance, which can be transformed to compliance by taking its reciprocal value.

References

- [1] Álvarez-Barrientos, F., Hurtado, D.E., Genet, M., 2021. Pressure-driven micro-poro-mechanics : A variational framework for modeling the response of porous materials. *International Journal of Engineering Science* 169, 103586.
- [2] Avilés-Rojas, N., Hurtado, D.E., 2022. Whole-lung finite-element models for mechanical ventilation and respiratory research applications. *Frontiers in Physiology* , 2060.
- [3] Bachofen, H., Schürch, S., 2001. Alveolar surface forces and lung architecture. *Comparative Biochemistry and Physiology Part A: Molecular & Integrative Physiology* 129, 183–193.
- [4] Bakhvalov, N., Panasenko, G., 1989. Homogenisation: Averaging Processes in Periodic Media. First edit ed., Kluwer Academic Publishers, Dordrecht/Boston/London.
- [5] Ball, L., Dameri, M., Pelosi, P., 2015. Modes of mechanical ventilation for the operating room. *Best Practice & Research Clinical Anaesthesiology* 29, 285–299.
- [6] Bates, J., Maksym, G., Navajas, D., Suki, B., 1994. Lung tissue rheology and 1/f noise. *Annals of biomedical engineering* 22, 674–681.
- [7] Berger, L., Bordas, R., Burrowes, K., Grau, V., Tavener, S., Kay, D., 2016. A poroelastic model coupled to a fluid network with applications in lung modelling. *International journal for numerical methods in biomedical engineering* 32.
- [8] Biot, M.A., 1941. General theory of three-dimensional consolidation. *Journal of applied physics* 12, 155–164.
- [9] Biot, M.A., 1955. Theory of elasticity and consolidation for a porous anisotropic solid. *Journal of applied physics* 26, 182–185.
- [10] Booth, A.J., Hadley, R., Cornett, A.M., Dreffs, A.A., Matthes, S.A., Tsui, J.L., Weiss, K., Horowitz, J.C., Fiore, V.F., Barker, T.H., et al., 2012. Acellular normal and fibrotic human lung matrices as a culture system for in vitro investigation. *American journal of respiratory and critical care medicine* 186, 866–876.
- [11] Burridge, R., Keller, J.B., 1981. Poroelasticity equations derived from microstructure. *The Journal of the Acoustical Society of America* 70, 1140–1146.
- [12] CGAL, . Computational Geometry Algorithms Library. URL: <http://www.cgal.org>.
- [13] Collis, J., Brown, D., Hubbard, M.E., O’Dea, R.D., 2017. Effective equations governing an active poroelastic medium. *Proceedings of the Royal Society A: Mathematical, Physical and Engineering Sciences* 473, 20160755.
- [14] Concha, F., Hurtado, D.E., 2020. Upscaling the poroelastic behavior of the lung parenchyma: A finite-deformation micromechanical model. *Journal of the Mechanics and Physics of Solids* 145, 104147.
- [15] Concha, F., Sarabia-Vallejos, M., Hurtado, D.E., 2018. Micromechanical model of lung parenchyma hyperelasticity. *Journal of the Mechanics and Physics of Solids* 112, 126–144.
- [16] Coussy, O., 2004. *Poromechanics*. John Wiley & Sons.
- [17] Dimbath, E., Maddipati, V., Stahl, J., Sewell, K., Domire, Z., George, S., Vahdati, A., 2021. Implications of microscale lung damage for covid-19 pulmonary ventilation dynamics: A narrative review. *Life Sciences* 274, 119341.
- [18] Dolhnikoff, M., Mauad, T., Ludwig, M.S., 1999. Extracellular matrix and oscillatory mechanics of rat lung parenchyma in bleomycin-induced fibrosis. *American Journal of Respiratory and Critical Care Medicine* 160, 1750–1757.
- [19] Fish, J., 2013. *Practical multiscale modeling*. John Wiley & Sons.
- [20] Fish, J., Fan, R., 2008. Mathematical homogenization of nonperiodic heterogeneous media subjected to large deformation transient loading. *International Journal for numerical methods in engineering* 76, 1044–1064.
- [21] Hess, D.R., 2014. Respiratory mechanics in mechanically ventilated patients. *Respiratory Care* 59, 1773–1794.
- [22] Hinz, B., 2012. Mechanical aspects of lung fibrosis: a spotlight on the myofibroblast. *Proceedings of the American Thoracic Society* 9, 137–147.

- [23] Hurtado, D.E., Castro, S., Madrid, P., 2017a. Uncertainty quantification of two models of cardiac electromechanics. *International Journal for Numerical Methods in Biomedical Engineering* 33, e2894.
- [24] Hurtado, D.E., Erranz, B., Lillo, F., Sarabia-Vallejos, M., Iturrieta, P., Morales, F., Blaha, K., Medina, T., Diaz, F., Cruces, P., 2020. Progression of regional lung strain and heterogeneity in lung injury: assessing the evolution under spontaneous breathing and mechanical ventilation. *Annals of intensive care* 10, 1–10.
- [25] Hurtado, D.E., Villarroel, N., Andrade, C., Retamal, J., Bugedo, G., Bruhn, A.R., 2017b. Spatial patterns and frequency distributions of regional deformation in the healthy human lung. *Biomechanics and Modeling in Mechanobiology* 16, 1413–1423.
- [26] Hurtado, D.E., Villarroel, N., Retamal, J., Bugedo, G., Bruhn, A., 2016. Improving the accuracy of registration-based biomechanical analysis: A finite element approach to lung regional strain quantification. *IEEE Transactions on Medical Imaging* 35, 580–588.
- [27] Hurtado, D.E., Zavala, P., 2021. Accelerating cardiac and vessel mechanics simulations : An energy-transform variational formulation for soft-tissue hyperelasticity. *Computer Methods in Applied Mechanics and Engineering* 379, 113764.
- [28] Kimmel, E., Boudiansky, B., 1990. Surface tension and the dodecahedron model for lung elasticity. *Journal of biomechanical engineering* 112, 160–167.
- [29] Kowalczyk, P., 1993. Mechanical model of lung parenchyma as a two-phase porous medium. *Transport in porous media* 11, 281–295.
- [30] Lévy, T., 1979. Propagation of waves in a fluid-saturated porous elastic solid. *International Journal of Engineering Science* 17, 1005–1014.
- [31] Logg, A., Mardal, K.A., Wells, G.N., et al., 2012. *Automated Solution of Differential Equations by the Finite Element Method*. Springer.
- [32] Lucangelo, U., Bernabé, F., Blanch, L., 2005. Respiratory mechanics derived from signals in the ventilator circuit. *Respiratory Care* 50, 55–65.
- [33] MacMinn, C.W., Dufresne, E.R., Wettlaufer, J.S., 2016. Large deformations of a soft porous material. *Physical Review Applied* 5, 044020.
- [34] Mead, J., 1961. Mechanical properties of lungs. *Physiological reviews* 41, 281–330.
- [35] Miller, L., Penta, R., 2021. Homogenized balance equations for nonlinear poroelastic composites. *Applied Sciences* 11, 6611.
- [36] Otis, D.R., Ingenito, E.P., Kamm, R.D., Johnson, M., 1994. Dynamic Surface-Tension of Surfactant Ta - Experiments and Theory. *Journal of Applied Physiology* 77, 2681–2688.
- [37] Papandrinopoulou, D., Tzouda, V., Tsoukalas, G., 2012. Lung compliance and chronic obstructive pulmonary disease. *Pulmonary medicine* 2012.
- [38] Parameswaran, H., Bartolák-Suki, E., Hamakawa, H., Majumdar, A., Allen, P.G., Suki, B., 2009. Three-dimensional measurement of alveolar airspace volumes in normal and emphysematous lungs using micro-ct. *Journal of Applied Physiology* 107, 583–592.
- [39] Patte, C., Brillet, P.Y., Fetita, C., Bernaudin, J.F., Gille, T., Nunes, H., Chapelle, D., Genet, M., 2022a. Estimation of Regional Pulmonary Compliance in Idiopathic Pulmonary Fibrosis Based on Personalized Lung Poromechanical Modeling. *Journal of Biomechanical Engineering* 144, 091008.
- [40] Patte, C., Genet, M., Chapelle, D., 2022b. A quasi-static poromechanical model of the lungs. *Biomechanics and Modeling in Mechanobiology* 21, 527–551.
- [41] Penta, R., Ambrosi, D., Shipley, R., 2014. Effective governing equations for poroelastic growing media. *Quarterly Journal of Mechanics and Applied Mathematics* 67, 69–91.
- [42] Perlman, C.E., Wu, Y., 2014. In situ determination of alveolar septal strain, stress and effective young’s modulus: an experimental/computational approach. *American Journal of Physiology-Lung Cellular and Molecular Physiology* 307, L302–L310.
- [43] Plantier, L., Cazes, A., Dinh-Xuan, A.T., Bancal, C., Marchand-Adam, S., Crestani, B., 2018. Physiology of the lung in idiopathic pulmonary fibrosis. *European Respiratory Review* 27, 1–14.
- [44] Pozin, N., Montesantos, S., Katz, I., Pichelin, M., Vignon-Clementel, I., Grandmont, C., 2017. A tree-parenchyma coupled model for lung ventilation simulation. *International journal for numerical*

- methods in biomedical engineering 33, e2873.
- [45] Quiros, K.A., Nelson, T.M., Sattari, S., Mariano, C.A., Ulu, A., Dominguez, E.C., Nordgren, T.M., Eskandari, M., 2022. Mouse lung mechanical properties under varying inflation volumes and cycling frequencies. *Scientific Reports* 12, 1–10.
 - [46] Raghu, G., Collard, H.R., Egan, J.J., Martinez, F.J., Behr, J., Brown, K.K., Colby, T.V., Cordier, J.F., Flaherty, K.R., Lasky, J.A., Lynch, D.A., Ryu, J.H., Swigris, J.J., Wells, A.U., Ancochea, J., Bouros, D., Carvalho, C., Costabel, U., Ebina, M., Hansell, D.M., Johkoh, T., Kim, D.S., King, T.E., Kondoh, Y., Myers, J., Müller, N.L., Nicholson, A.G., Richeldi, L., Selman, M., Dudden, R.F., Griss, B.S., Protzko, S.L., Schünemann, H.J., 2011. An Official ATS/ERS/JRS/ALAT Statement: Idiopathic pulmonary fibrosis: Evidence-based guidelines for diagnosis and management. *American Journal of Respiratory and Critical Care Medicine* 183, 788–824.
 - [47] Roth, C.J., Ismail, M., Yoshihara, L., Wall, W.A., 2017a. A comprehensive computational human lung model incorporating inter-acinar dependencies: Application to spontaneous breathing and mechanical ventilation. *International journal for numerical methods in biomedical engineering* 33, e02787.
 - [48] Roth, C.J., Yoshihara, L., Ismail, M., Wall, W.A., 2017b. Computational modelling of the respiratory system: discussion of coupled modelling approaches and two recent extensions. *Computer Methods in Applied Mechanics and Engineering* 314, 473–493.
 - [49] Saad, S.M., Neumann, A.W., Acosta, E.J., 2010. A dynamic compression–relaxation model for lung surfactants. *Colloids and Surfaces A: Physicochemical and Engineering Aspects* 354, 34–44.
 - [50] Sarabia-Vallejos, M.A., Ayala-jeria, P., Hurtado, D.E., 2021. Three-Dimensional Whole-Organ Characterization of the Regional Alveolar Morphology in Normal Murine Lungs. *Frontiers in Physiology* 12, 1–11.
 - [51] Sarabia-Vallejos, M.A., Zuñiga, M., Hurtado, D.E., 2019. The role of three-dimensionality and alveolar pressure in the distribution and amplification of alveolar stresses. *Scientific Reports* 9, 8783.
 - [52] Snijder, J., Peraza, J., Padilla, M., Capaccione, K., Salvatore, M.M., 2019. Pulmonary fibrosis: a disease of alveolar collapse and collagen deposition. *Expert review of respiratory medicine* 13, 615–619.
 - [53] Suki, B., Sato, S., Parameswaran, H., Szabari, M.V., Takahashi, A., Bartolak-Suki, E., 2013. Emphysema and Mechanical Stress-Induced Lung Remodeling. *Physiology* 28, 404–413.
 - [54] Suki, B., Stamenović, D., Hubmayr, R., 2011. Lung parenchymal mechanics. *Comprehensive Physiology* 1, 1317–1351.
 - [55] Swan, A.J., Clark, A.R., Tawhai, M.H., 2012. A computational model of the topographic distribution of ventilation in healthy human lungs. *Journal of theoretical biology* 300, 222–231.
 - [56] Tawhai, M.H., Bates, J.H., 2011. Multi-scale lung modeling. *Journal of Applied Physiology* 110, 1466–1472.
 - [57] Upagupta, C., Shimbori, C., Alsilmi, R., Kolb, M., 2018. Matrix abnormalities in pulmonary fibrosis. *European Respiratory Review* 27.
 - [58] Wall, W.A., Wiechert, L., Comerford, A., Rausch, S.M.K., 2010. Towards a comprehensive computational model for the respiratory system. *International Journal for Numerical Methods in Biomedical Engineering* 26, 807–827.
 - [59] Wiechert, L., Wall, W., 2010. A nested dynamic multi-scale approach for 3d problems accounting for micro-scale multi-physics. *Computer Methods in Applied Mechanics and Engineering* 199, 1342–1351.